

Theoretical and Experimental Studies of CO₂ and H₂ Separation Using the 1-Ethyl-3-methylimidazolium Acetate ([emim][CH₃COO]) Ionic Liquid

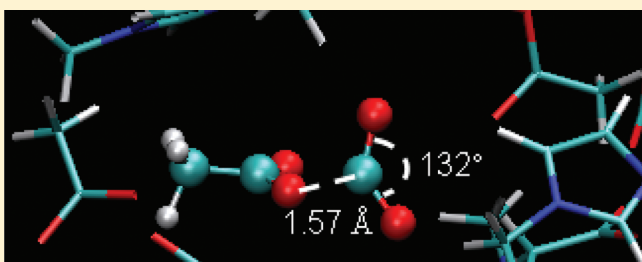
Wei Shi,^{*,†,‡,§} Christina R. Myers,[†] David R. Luebke,^{*,†} Janice A. Steckel,[†] and Dan C. Sorescu[†]

[†]National Energy Technology Laboratory, U.S. Department of Energy, Pittsburgh, Pennsylvania 15236, United States

[‡]URS Corporation, South Park, Pennsylvania 15129, United States

[§]Department of Chemical and Petroleum Engineering, University of Pittsburgh, Pittsburgh, Pennsylvania 15261, United States

ABSTRACT: The performance of [emim][CH₃COO] ionic liquid (IL) to separate mixtures of CO₂ and H₂ is studied using both classical and ab initio simulation methods and experiments. Simulations show that H₂ solubility and permeability in [emim][CH₃COO] are quite low with Henry's law constants about 1×10^4 bar and permeabilities in the range 29–79 barrer at 313–373 K. In the case of CO₂ absorption in [emim][CH₃COO], ab initio molecular dynamics simulations predict two types of CO₂ absorption states. In type I state, CO₂ molecules interact with the [CH₃COO][−] anion through strong complexation leading to high CO₂ solubility. The C atom of CO₂ is located close to the O atoms of the [CH₃COO][−] anion with an average distance of about 1.61 Å. The CO₂ bond angle ($\theta(\text{OCO})$) is about 138°, significantly perturbed from that of an isolated linear CO₂. In type II state, the CO₂ molecule maintains a linear configuration and is located at larger separations (>2.2 Å) from the [CH₃COO][−] anion. The weaker interaction of CO₂ with the [CH₃COO][−] anion in type II state is similar to the one observed when CO₂ absorbs in [bmim][PF₆]. Simulations further demonstrate that the [emim]⁺ cation competes with CO₂ to interact with the [CH₃COO][−] anion. The predicted high CO₂ permeability and low H₂ permeability in [emim][CH₃COO] are also verified by our experiments. The experimental CO₂ permeability in [emim][CH₃COO] is in the range of 1325–3701 barrer, and high experimental CO₂/H₂ permeability selectivities of 21–37 at 313–373 K are observed. We propose that by replacing [emim]⁺ cation with 1-butyl-1-methylpyrrolidinium ([PY₁₄]⁺) further enhancement of CO₂ solubility in [PY₁₄][CH₃COO] IL will be obtained as well as good performance to separate CO₂ and H₂.



1. INTRODUCTION

Ionic liquids (ILs) are of interest for a variety of gas separation applications but the most interest they received is in selective separations of CO₂. While separations of CO₂ from N₂-containing streams are of primary interest in conventional power generation applications, separations of CO₂ from mixtures containing H₂ are also of great interest for coal gasification. In either of these systems, ILs may be used as regenerable solvents or as the transport phase in supported liquid membranes. For solvent applications, CO₂ solubility is the primary performance property of interest. In membranes, CO₂ permeability and CO₂/H₂ permeability selectivity are the critical performance metrics.

The IL 1-butyl-3-methylimidazolium acetate ([bmim][CH₃COO]) was first reported by Maginn et al.¹ to show high CO₂ solubility. Chinn et al.² later proposed a solvent made up of [bmim][CH₃COO] and water for CO₂ capture. Recently, Shiflett et al.^{3–5} have extensively studied ILs based on acetate-like anions and they have demonstrated desirable separation properties including high CO₂ solubility. To better understand the source of this high CO₂ solubility, Bhargava et al.⁶ performed ab initio gas-phase calculations and found that the interaction energy between CO₂ and the [CH₃COO][−] anion is about 11 kJ/mol stronger than that between CO₂ and the [CF₃COO][−] anion, consistent with the

higher CO₂ solubility in [emim][CH₃COO] compared to [emim][CF₃COO]. Carvalho et al.⁷ have also performed both experimental and theoretical studies and they have found that CO₂ solubility in [bmim][CH₃COO] is much higher than in [bmim][CF₃COO], consistent with their calculations that in the gas phase CO₂ interacts with [CH₃COO][−] anion about 8–10 kJ/mol stronger than with [CF₃COO][−] anion. A more relevant question for practical applications is how CO₂ interacts with acetate-based ILs in the condensed phase?

H₂ absorption properties are also important to evaluate ILs' performance to separate CO₂ from mixtures containing H₂. In a previously published work,⁸ we have shown that H₂ solubility is highly dependent upon the molar volume of the IL. Indeed, ILs which physically absorb CO₂ through simple van der Waals (VDW) and electrostatic (ELEC) interactions are not ideal systems to separate mixtures of CO₂ and H₂ because the CO₂ solubility is largely dependent upon the IL molar volume leading to a small CO₂/H₂ solubility selectivity. We have proposed to use ILs with small molar volume (leading to low H₂ solubility), which

Received: June 21, 2011

Revised: October 10, 2011

Published: December 01, 2011

interact strongly with CO₂. These characteristics are expected to show high CO₂ solubility and high CO₂/H₂ selectivity.⁸

In this work, we focus on analysis of CO₂ absorption in [emim][CH₃COO], and the performances of this IL to separate mixtures of CO₂ and H₂ using both simulations and experiments. This IL seems to be an ideal candidate based on both its very small molar volume, ~154 cm³/mol at 298 K,⁵ and high CO₂ solubility. Theoretical analysis has been performed using several computational techniques. First, ab initio calculations were used to obtain an accurate description of the interaction of H₂ and CO₂ with the [CH₃COO][−] anion. Extension of our analysis to the condensed phase has been obtained by performing ab initio molecular dynamics simulations for the case of CO₂ absorption in the [emim][CH₃COO] ionic liquid. Finally, classical Monte Carlo (MC) and molecular dynamics (MD) simulations were used to quantitatively compute H₂ solubility, diffusivity, and permeability in [emim][CH₃COO]. Simulations in this case were done using a classical force field capable to describe the weak interactions between H₂ and ionic liquids of interest. For comparison, we also performed ab initio molecular dynamics simulations for H₂ absorption in [emim][CH₃COO] and CO₂ absorption in [emim][PF₆]. In the case of the proposed ionic liquid [PY₁₄][CH₃COO], similar to the case of [emim][CH₃COO], classical simulations were used for H₂ to study gas solubility and diffusion properties while ab initio molecular dynamics simulations were applied to study CO₂ absorption in [PY₁₄][CH₃COO]. Our theoretical predictions were further verified through experiments by measurements of CO₂ and H₂ permeabilities in [emim][CH₃COO].

2. SIMULATION METHODS

2.1. Classical Force Field. A classical force field has been used to simulate ILs, solute molecules, and the interaction between ILs and the solute molecules in basin-hopping (BH) calculations, classical MC and MD simulations as described below. In all these instances the interaction energy is given by,

$$\begin{aligned} \mathcal{V}(\mathbf{r}) = & \sum_{\text{bonds}} k_b(r - r_0)^2 + \sum_{\text{angles}} k_\theta(\theta - \theta_0)^2 \\ & + \sum_{\text{dihedrals}} k_\chi[1 + \cos(n_\chi\chi - \delta_0)] \\ & + \sum_{\text{impropers}} k_\psi(\psi - \psi_0)^2 \\ & + \sum_{i=1}^{N-1} \sum_{j=i+1}^N \left\{ 4\epsilon_{ij} \left[\left(\frac{\sigma_{ij}}{r_{ij}} \right)^{12} - \left(\frac{\sigma_{ij}}{r_{ij}} \right)^6 \right] + \frac{q_i q_j}{r_{ij}} \right\} \end{aligned} \quad (1)$$

where the symbols have their conventional meaning.⁹ Standard Lorentz–Berthelot combining rules were used to calculate the mixed Lennard–Jones (LJ) interaction parameters. The LJ potential was switched from 10.5 to 12.0 Å. A Verlet neighbor list with a 13.5 Å radius was used. The intramolecular electrostatic and LJ interactions for atoms separated by exactly three consecutive bonds were scaled by 0.5 and were neglected for atoms separated by less than three consecutive bonds. The classical force field parameters for CO₂, [Tf₂N][−], [PF₆][−], [hmim]⁺, and [emim]⁺ were obtained from previous work.^{10–13} For the [PY₁₄]⁺ cation, most of the force field parameters were obtained from the work by Padua et al.¹⁴ except the charges of [PY₁₄]⁺

Table 1. Force Field Parameters Used in This Work for the [CH₃COO][−] Anion^a

atom	q_i (e)	ϵ_i (K)	σ_i (Å)
O	−0.861	105.675	2.96
C (C–O)	0.972	52.838	3.75
C (CH ₃)	−0.25	33.212	3.5
H (CH ₃)	0.0	7.548	2.42
atom–atom bond	k_b (kcal/mol Å ^{−2})	r_0 (Å)	
C–C	247.5	1.542	
C–O	619.0	1.256	
C–H	373.0	1.089	
atom–atom–atom angle	k_θ (kcal/mol rad ^{−2})	θ_0 (deg)	
O–C–O	131.0	128.831	
O–C–C	106.5	115.585	
C–C–H	45.5	110.017	
H–C–H	45.0	108.897	
dihedral	k_χ (kcal/mol)	n_θ	δ_0 (deg)
H–C–C–O	0.0089	6	0.00

^a The symbols correspond to those in eq 1.

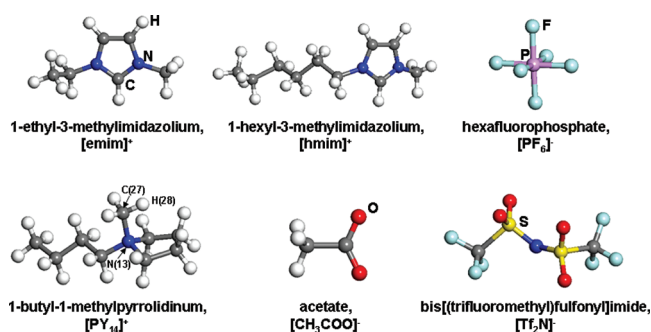


Figure 1. Molecular structures for cations and anions studied in this work. Also shown are the full chemical names and abbreviations for the ions. In the case of the [PY₁₄]⁺ cation, three atoms which are described in the text are also indicated and labeled in the figure.

which were computed in this work at the B3LYP/6-311++G(d,p) level. The two-atom center of the Cracknell model¹⁵ was used for H₂.

For the [CH₃COO][−] anion, the LJ parameters were set to be the same as for the neutral acetic acid molecule.¹⁶ Equilibrium bond length (r_0) and angles (θ_0) were obtained from geometry optimization at the B3LYP/6-311+G* level of theory. Bond force constants were obtained directly from the force constant matrix calculated at the B3LYP/6-311+G* level of theory and scaled by a factor of 0.966.¹⁷ Angle force constants were derived by doing a series of structural perturbations of the optimized structure where the angles were incremented by $\pm 2^\circ$, followed by single-point energy calculations at the B3LYP/6-311+G* level. The angle force constants were derived assuming a harmonic approximation. Charges were calculated using the CHELPG protocol on the optimized [CH₃COO][−] anion. The dihedral parameters for the H–C–C–O torsional angles were obtained through a scanning procedure and fitted to the cosine form indicated in eq 1. All the parameters for the [CH₃COO][−] anion used in this

work are summarized in Table 1. All cations and anions studied in this work are shown in Figure 1.

2.2. Details for Basin-Hopping Calculations. The basin-hopping method is a powerful technique to find the global minima for a wide variety of functions.^{18,19} The method works by locating and comparing the local minima and determining the acceptance of those minima using a Monte Carlo-type procedure. Our implementation of the BH method was described in a previous publication.²⁰ In this work, BH calculations were used to obtain the lowest local minima for dimers containing one CO₂ or H₂ molecule and one ion. After the lowest energy for the dimer was identified, the interaction energy between the gas molecule and the ion was computed as the difference between the total energy for the optimized dimer and the sum of energies for the respective monomers at the optimized dimer structure. Note that full electrostatic interactions were computed during simulations.

2.3. Details for Monte Carlo and Molecular Dynamics Simulations. Simulation details for continuous fractional component (CFC) MC simulations for solubility calculations and MD simulations to compute self-diffusivity are similar to those employed in the previous work.^{8,12} H₂ solubility in the system of 160 anion/cation pairs was studied using the CFC MC simulations performed at temperatures ranging from 313 to 373 K and pressures ranging from 200 to 400 bar. Typically, one million equilibration steps were performed followed by 10 to 20 million steps of production runs. In the case of constant energy NVE MD simulations, the production runs were set to be 10–20 ns long with time steps of 0.5–1.0 fs. Self-diffusivity coefficients were estimated from the NVE simulation trajectories using the Einstein relation as described in our previous work.⁸ The MD simulations were performed in the temperature range 313–373 K for systems consisting of 160 IL pairs and five H₂ molecules. We have used the Ewald⁹ technique in MD simulations and the Fennel and Gezelter shift force²¹ method in MC simulations to calculate the electrostatic interactions.

2.4. Details for Ab Initio (AI) Quantum Calculations. Ab initio quantum calculations have been performed at different levels of theory (BLYP/aug-cc-pVQZ, MP2/cc-pVTZ, RI-MP2/aug-cc-pVTZ, and RI-MP2/aug-cc-pVQZ) and charges were determined using the CHELPG protocol.²² To account for the basis set superposition error, we have used counterpoise corrections in both structural optimizations and frequency calculations. The majority of calculations were performed using the Gaussian 03 program¹⁷ while RI-MP2 calculations were performed using the Q-Chem²³ package. The dimers systems studied include CO₂–[CH₃COO][–], CO₂–[PF₆][–], CO₂–[Tf₂N][–], CO₂–[hmim]⁺, H₂–[CH₃COO][–], H₂–[PF₆][–], H₂–[Tf₂N][–], and H₂–[hmim]⁺. For the CO₂–[CH₃COO][–] system, several different CO₂ positions relative to the anion, were tried. In the cases of CO₂ and H₂ interacting with the [hmim]⁺ cation, two different initial configurations have been examined in the AI calculations and only the optimized structures with the lowest energies are reported in this work.

2.5. Details for Ab Initio Molecular Dynamics Simulations. Ab initio molecular dynamics simulations using the CPMD^{24,25} (version 3.13.2) program were performed for four systems: CO₂–[emim][CH₃COO], CO₂–[emim][PF₆], CO₂–[PY₁₄][CH₃COO] and H₂–[emim][CH₃COO]. All four systems contained 10 gas molecules and 10 IL pairs. The CO₂–[emim][CH₃COO] system consists of 290 atoms in a cubic box with the edge length of 13.807 Å, roughly corresponding to the pure IL density of 1.101 g/cm³⁵ at 298 K. The H₂–[emim][CH₃COO]

system contains 280 atoms in the same simulation box as that for the CO₂–[emim][CH₃COO] system. Simulations for the CO₂–[emim][CH₃COO] and H₂–[emim][CH₃COO] systems were performed at 298 K. In the case of CO₂–[emim][PF₆], the system contains 290 atoms in a cubic box with an edge length of 14.419 Å, leading to an IL density close to the experimental value of 1.422 g/cm³ at 353 K.²⁶ Simulations for this system were performed at 353 K. The CO₂–[PY₁₄][CH₃COO] system contains 400 atoms and the simulation box size is 15.22 Å.

The BLYP exchange-correlation functional and norm-conserving pseudopotentials of the Troullier-Martins form were employed. Deuterium was used to substitute for all hydrogen atoms in the system to enable a larger time step of 5 au (about 0.12 fs). The fictitious electron mass was set to be 700 au. The Nosé–Hoover chain thermostat was applied to control the temperature. The energy cutoff for the plane wave basis set was chosen to be 90 Ry. A typical 1.2 ps NVE run was initially performed for equilibration followed by 12 ps NVT production runs for structural analysis.

We have also studied the effect of using different functionals by considering PBE functional with Troullier-Martins type pseudopotentials, while the other simulation parameters were kept the same as for the BLYP functional case. For a number of condensed-phase configurations the atomic charges have been computed using the ESP procedure^{27,28} available in the CPMD program.

3. EXPERIMENTAL DETAILS FOR THE SUPPORTED IONIC LIQUID MEMBRANE

The IL [emim][CH₃COO] was obtained from Sigma-Aldrich and used without further purification. The IL has a purity higher than 96.5% with water concentration less than 0.1%. The water content of 0.1% was the manufacturer's specification. Since the time of submission, water content has been measured using the Karl Fischer Water Testing Method ASTM D6304 and found to be 0.3 ± 0.1%. The purity was the manufacturer's specification which was confirmed prior to shipment by refractometry and ion chromatography. Manufacturer specifications also indicated that bromide (Br[–]), chloride (Cl[–]), nitrate (NO₃[–]), phosphate (PO₄^{3–}), and sulfate (SO₄^{2–}), which are the common anionic precursors, were less than 0.0025% per anion, respectively. The exact nature of the impurities was not characterized. The absence of the precursors indicates that complete anionic exchange has occurred. In most imidazolium-based ionic liquids, small amounts of cationic impurities are present because purification of the imidazolium precursors is difficult. These cationic precursors are similar in nature to the desired cation and as a result are not expected to interact with the acetate anion in a way that will substantially affect experimental performance.

Since water content is known to significantly affect the performance of acetate-based ILs, supported ionic liquid membranes (SILMs) were prepared in a glovebox under dry nitrogen with water concentration less than 300 ppm. In a shallow dish, a sufficient quantity of [emim][CH₃COO] was deposited to cover a porous polysulfone disk. The membrane was allowed to absorb the IL for at least 4 h. The membrane was then removed from the IL and blotted dry. Still in the glovebox, the SILM was placed in a commercially available Millipore Stainless Steel Filter Holder and sealed for transport to the permeability testing system. Constant pressure membrane performance testing was carried out with equipment and procedures which have been previously

Table 2. Molar Volume V_m and the Density ρ Obtained from NPT Simulations for [emim][CH₃COO] at 298.2–373.2 K and 1 bar^a

T (K)	$V_m(\text{sim})$ (cm ³ /mol)	$\rho(\text{sim})$ (g/cm ³)	$\rho(\text{expt})^5$ (g/cm ³)
298.2	158.5 (1)	1.074 (1)	1.102
313.2	160.50 (6)	1.0605 (4)	1.092
348.2	163.44 (6)	1.0415 (4)	1.073
373.2	166.5 (1)	1.0223 (6)	1.059

^aThe experimental density⁵ is also included for comparison. The uncertainty from the simulations in the last digit is given in parentheses.

reported.²⁹ CO₂ and H₂ permeabilities and CO₂/H₂ selectivity were evaluated in a mixture containing 20.02 mol % CO₂, 19.99% H₂, and a balance of 59.99% argon. An inert sweep gas, in this case Ar, is employed on the permeate side of the membrane to keep the concentrations of the permeating species there, in this case H₂ and CO₂, near zero. To minimize the effect of any back diffusion of Ar and allow for convenient gas analysis of the feed stream after contact with the membrane, the CO₂/H₂ mixture is diluted with Ar.

Prior work in transport of gases through ionic liquid membranes has shown little difference between pure and mixed gas properties.³⁰ Cosolubility and cosorption effects appear to be insubstantial in ionic liquid membranes, particularly at low pressures and when the mixture components are low-solubility gases such as H₂ and Ar. It is, therefore, believed that the comparison of experimental mixed gas transport properties to simulated pure gas properties should be valid.

Experimental results reported in this work are 2-fold. On one side the experimental data related to H₂ permeability in [emim][CH₃COO] was obtained and used to compare with our theoretical results. Second, the experimental results also demonstrated that CO₂ has a high permeability in the [emim][CH₃COO] ionic liquid. However, in this second case, theoretical predictions were limited due to the limitations of our classical force field to accurately describe the strong interactions between CO₂ molecule and the [CH₃COO][−] anion as shown later.

4. RESULTS AND DISCUSSION

4.1. Simulated Densities for [emim][CH₃COO]. To test the accuracy of the classical force field parameters for the [CH₃COO][−] anion developed in this work (see Table 1), the density of the IL [emim][CH₃COO] was calculated at various temperatures and at a pressure of 1 bar. The results are shown in Table 2. The differences between the simulated and experimentally determined density values⁵ range from 2.5 to 3.5%. The density difference between simulations and experiments can be partially explained by the fact that experimental IL purity was only 96.5%. The small differences indicate that the force field parameters for [CH₃COO][−] are reasonably accurate in predicting the volume of the IL. These force field parameters for the [CH₃COO][−] anion were subsequently used in our classical BH, MD, and MC simulations.

4.2. Results for CO₂. **4.2.1. AI and BH Gas-Phase Calculations.** *Optimized Structures.* The optimized structures for the CO₂–[CH₃COO][−] and CO₂–[PF₆][−] systems as determined from AI calculations are compared to the structures derived from BH calculations and are shown in Figure 2. In the case of the

CO₂–[CH₃COO][−] system, AI calculations using different levels of theory (BLYP and RI-MP2) and different basis sets give two types of binding configurations, i.e., η^1 and η^2 configurations. In η^1 , the CO₂ molecule interacts with one oxygen atom of the [CH₃COO][−] anion and the CO₂ molecule is significantly distorted from a linear configuration. In η^2 configuration, CO₂ molecule interacts with both oxygen atoms of the anion and CO₂ molecule exhibits a more linear-like configuration. The BH calculations using the classical force field predict an optimized structure similar to η^2 but fail to predict the bent structure η^1 . As shown in Table 3 for the η^1 configuration, AI calculations show that there is a significant charge transfer from the [CH₃COO][−] anion to the CO₂ molecule of about $-0.4e$. This significant charge transfer is missing in our classical force field and hence the classical simulations fail to predict the η^1 configuration. In the case of η^2 structure, the charge transfer is only about $-0.1e$, significantly smaller compared to that in η^1 . This binding state is qualitatively predicted by our classical force field.

For the CO₂–[PF₆][−] system, the structures obtained from the AI and BH calculations are quite similar. The strong similarities between the two structures indicate that the classical force field parameters used for CO₂ and [PF₆][−] effectively predict the optimized structure obtained in AI calculations. Similar to the η^2 case, the agreement between AI and BH calculation is partly due to the small charge transfer from the [PF₆][−] anion to the CO₂ molecule (see Table 3). The structures for the CO₂–[Tf₂N][−] and CO₂–[hmim]⁺ systems as obtained from AI and BH calculations (not shown here) also compare well with each other.

Interaction and Binding Energies. Other properties of interest we analyzed are the binding energy and the interaction energy in the CO₂–[CH₃COO][−] dimer system (see Table 3). The binding energy is defined as the energy required to form a dimer when bringing together two monomers from an infinitely large separation. By contrast, the interaction energy is the energy required to separate two monomers of a dimer to an infinitely large distance but keeping the monomers structure frozen at their geometries in the optimized dimer system. Both these two energies are important to determine the gas solubility.³¹ Except for the η^1 configuration in the CO₂–[CH₃COO][−] case, the difference between the binding and the interaction energies is typically small. This is due to the fact that CO₂ and H₂ structures in the optimized dimers are not significantly different from the respective optimized monomers. In contrast, for the η^1 state in the CO₂–[CH₃COO][−] system, CO₂ is significantly bent and the CO₂–[CH₃COO][−] interaction energy is about 140–150 kJ/mol stronger than the binding energy. We note that the binding energies for η^1 and η^2 structures are similar with a difference of only 12 kJ/mol. However, the interaction energy in η^1 is about 126–136 kJ/mol stronger than that in η^2 . It is this strong interaction energy in η^1 configuration (referred to as complexation interaction in this work) that contributes to the high CO₂ solubility in the [emim][CH₃COO] IL, as will be shown later in ab initio molecular dynamics simulations.

Excepting the η^1 configuration in the CO₂–[CH₃COO][−] system, both the AI and BH calculations show that the interaction between CO₂ and the [CH₃COO][−] anion is about 36%–151% stronger than that between CO₂ and the other two anions, [PF₆][−] and [Tf₂N][−]. In the case of η^1 configuration for the CO₂–[CH₃COO][−] system, the CO₂ interaction with the [CH₃COO][−] anion is about 7–10 times stronger than with

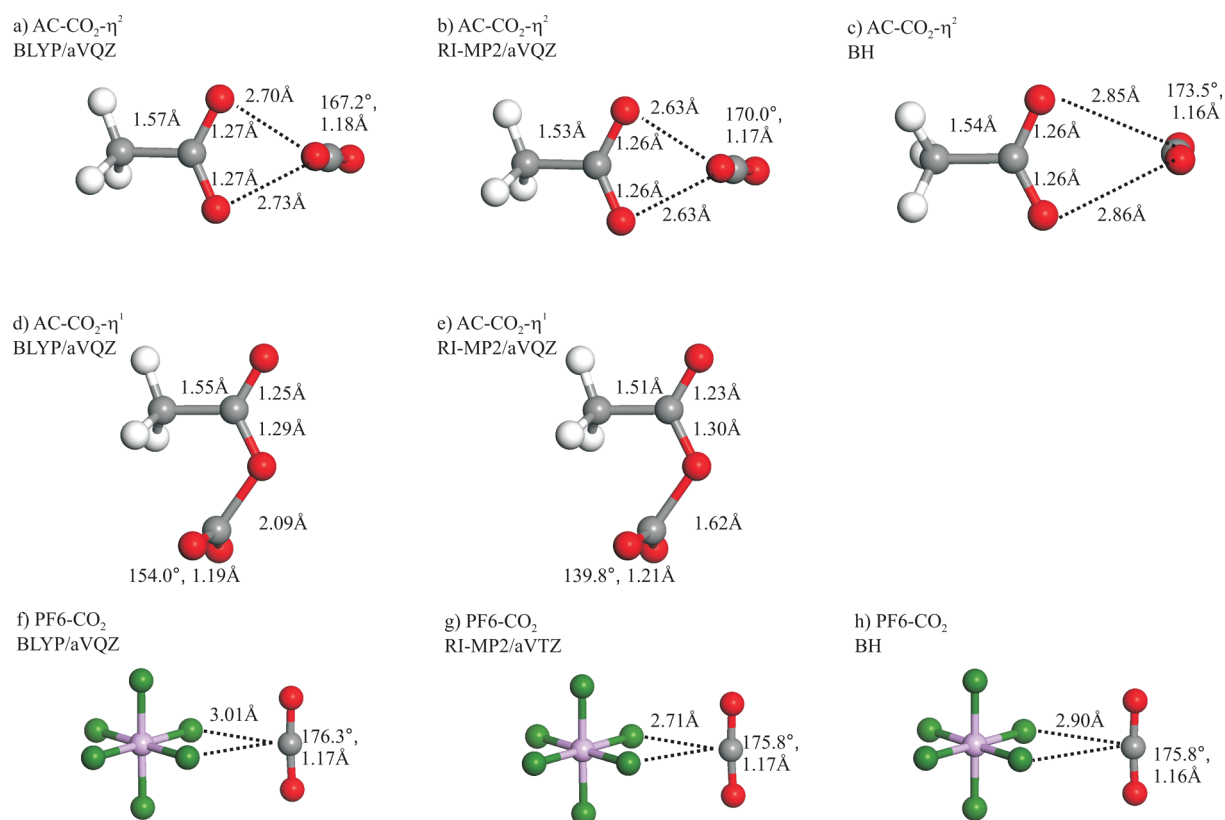


Figure 2. Optimized structures of $\text{CO}_2\text{--}[\text{CH}_3\text{COO}]^-$ and $\text{CO}_2\text{--}[\text{PF}_6]^-$ as obtained from ab initio gas calculations and basin-hopping (BH) calculations using a classical force field. For the $\text{CO}_2\text{--}[\text{CH}_3\text{COO}]^-$ system, two different optimized structures (η^1 with a highly bent CO_2 structure and η^2 with a more linear CO_2 structure) obtained from the RI-MP2/aug-cc-pVQZ (aVQZ) and BLYP/aug-cc-pVQZ methods are shown.

Table 3. Comparison of the Interaction (INT) Energies Determined Using Ab Initio (AI) Methods at RI-MP2 (INT1) and MP2/cc-pVTZ (INT2) Levels and BH Calculations Using the Classical Force Field for Various Dimer Systems^a

system	AI INT (kJ/mol)		AI BIND1 (kJ/mol)	AI Q (+e) solute	BH (kJ/mol) INT energy	BH (kJ/mol)	
	INT1	INT2				VDW	ELEC
$\text{CO}_2\text{--}[\text{CH}_3\text{COO}]^- (\eta^2)$	−50.5	−45.7	−43.2	−0.12	−34.4	−2.4	−32.0
$\text{CO}_2\text{--}[\text{CH}_3\text{COO}]^- (\eta^1)$	−177	−182	−31.1	−0.43	NA	NA	NA
$\text{CO}_2\text{--}[\text{PF}_6]^-$	−21.2	−18.2	−19.6	−0.05	−17.6	−3.6	−14.0
$\text{CO}_2\text{--}[\text{Tf}_2\text{N}]^-$	−26.0	−22.0	−24.9	−0.04	−25.3	−6.3	−19.0
$\text{CO}_2\text{--}[\text{hmim}]^+$	−17.2	−16.6	−16.2	0.03	−14.2	−4.9	−9.3
$\text{H}_2\text{--}[\text{CH}_3\text{COO}]^-$	−11.6	−10.9	−11.3	−0.06	−1.8	−1.8	0.0
$\text{H}_2\text{--}[\text{PF}_6]^-$	−5.1	−4.9	−5.1	−0.02	−1.6	−1.6	0.0
$\text{H}_2\text{--}[\text{Tf}_2\text{N}]^-$	−4.6	−4.3	−4.6	−0.03	−4.0	−4.0	0.0
$\text{H}_2\text{--}[\text{hmim}]^+$	−4.9	−3.3	−4.9	0.03	−3.1	−3.1	0.0

^a Also shown in the table are the binding energies from RI-MP2 (BIND1) calculations, the CHelpG charges (Q) for CO_2 and H_2 obtained at the MP2/cc-pVTZ level in the dimer, and the van der Waals (VDW) and electrostatic (ELEC) interactions between CO_2 , H_2 , and the ions as determined in BH calculations. For the $\text{CO}_2\text{--}[\text{CH}_3\text{COO}]^-$ dimer system, the AI methods corresponding to two binding states (η^1) and (η^2) are indicated (see Figure 2). In this case, the classical force field fails to predict the η^1 structure and hence the corresponding results are denoted as NA. In the case of RI-MP2 calculations, the basis sets are aug-cc-pVQZ for dimer systems containing $[\text{CH}_3\text{COO}]^-$ anion, aug-cc-pVTZ for the dimer system containing the $[\text{PF}_6]^-$ and $[\text{Tf}_2\text{N}]^-$ anions, and cc-pVTZ for the $[\text{hmim}]^+$ cation.

the $[\text{PF}_6]^-$ and $[\text{Tf}_2\text{N}]^-$ anions. All these calculations are consistent with the higher CO_2 solubility in ILs containing the $[\text{CH}_3\text{COO}]^-$ anion,^{3–5} such as $[\text{emim}][\text{CH}_3\text{COO}]$ and $[\text{bmim}][\text{CH}_3\text{COO}]$, relative to ILs containing $[\text{Tf}_2\text{N}]^-$ ^{3,12} and $[\text{PF}_6]^-$ ^{32,33} anions, such as $[\text{emim}][\text{Tf}_2\text{N}]$, $[\text{hmim}][\text{Tf}_2\text{N}]$, $[\text{emim}][\text{PF}_6]$, and $[\text{bmim}][\text{PF}_6]$. Our findings of a stronger interaction between CO_2 and

the $[\text{CH}_3\text{COO}]^-$ anion compared to the $[\text{PF}_6]^-$ and $[\text{Tf}_2\text{N}]^-$ anions are also consistent with previous results obtained by Bhargava et al.⁶

In the case of the $[\text{hmim}]^+$ cation, both AI and BH calculations show that the interaction with CO_2 is weaker than interaction of CO_2 with three other anions ($[\text{CH}_3\text{COO}]^-$, $[\text{PF}_6]^-$, $[\text{Tf}_2\text{N}]^-$).

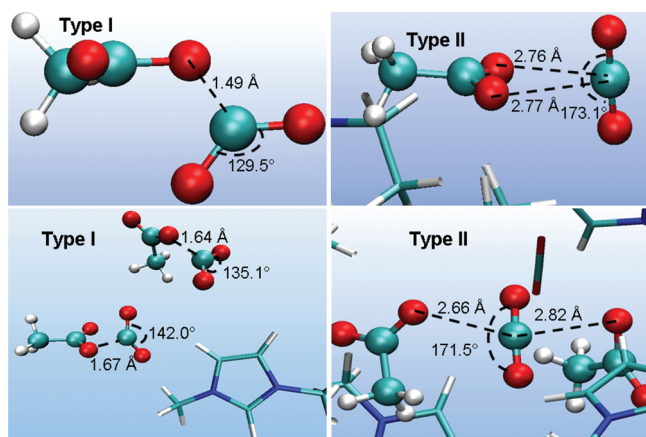


Figure 3. Snapshots from CPMD simulations for CO_2 absorption in $[\text{emim}][\text{CH}_3\text{COO}]$ showing two types of CO_2 absorption states. For clarity, many atoms in the system are left out and are not shown in the figure. In both type I and type II CO_2 absorption states, two snapshots with different CO_2 configurations relative to the $[\text{CH}_3\text{COO}]^-$ anions are shown.

This behavior is partly due to the basicity of the anion and the acidity of both the CO_2 and the cation. For all three anions and the cation, simulations in the gas phase show that the ELEC interactions with CO_2 are much stronger than the VDW interactions.

Comparison of AI and BH Interaction Energies. When comparing the interaction energies obtained from the AI and BH calculations, it is clearly shown in Table 3 that the difference between AI and BH is small for the $\text{CO}_2-[\text{PF}_6]^-$, $\text{CO}_2-[\text{Tf}_2\text{N}]^-$, and $\text{CO}_2-[\text{hmim}]^+$ systems. The absolute differences in interaction energy between the AI and BH calculations are typically less than 3 kJ/mol with relative differences of 3–15%. Considering the similar optimized dimer structures and the small energy differences between the AI and the BH calculations for these three systems, it follows that the classical force field is useful in predicting CO_2 sorption in these ILs. This conclusion is also consistent with previous simulated solubility results using the same force field parameters which showed a good agreement with experimental data for CO_2 absorption in $[\text{hmim}][\text{Tf}_2\text{N}]$.¹²

In the case of the $\text{CO}_2-[\text{CH}_3\text{COO}]^-$ system, the classical force field fails to predict the η^1 structure. Indeed, our simulated CO_2 solubilities in $[\text{emim}][\text{CH}_3\text{COO}]$ performed at 348 K and pressures 1–20 bar using the classical force field are 4–19 times smaller than the experimental value.⁵ Note that the BH and AI calculations give similar interaction energies and optimized structures for the $\text{CO}_2-[\text{emim}]^+$ system (not shown here). Hence, the observed difference between the simulated CO_2 solubility and the experimental data is mainly due to the classical force field's underestimation of the interaction between CO_2 and the $[\text{CH}_3\text{COO}]^-$ anion. To predict CO_2 solubility in the types of ILs containing $[\text{CH}_3\text{COO}]^-$ -like anions, a new force field model must be developed to accurately describe strong CO_2 interactions and the corresponding charge transfer that was observed in AI calculations, particular for the η^1 configuration.

4.2.2. CPMD Simulations of $\text{CO}_2-[\text{emim}][\text{CH}_3\text{COO}]$ and $\text{CO}_2-[\text{emim}][\text{PF}_6]$ Systems. Type I and II CO_2 Absorption States in $[\text{emim}][\text{CH}_3\text{COO}]$. Since the current available classical force field underestimates the interaction between CO_2 and the $[\text{CH}_3\text{COO}]^-$ anion as shown above, CPMD simulations were

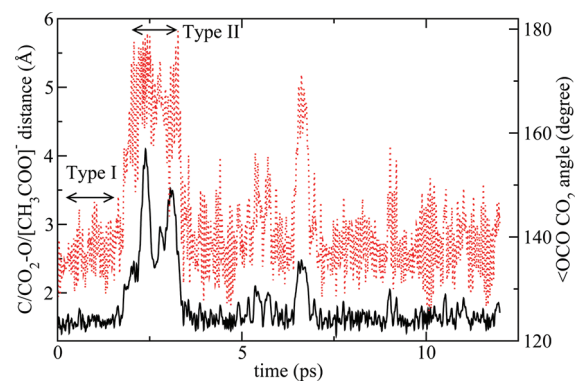


Figure 4. Distance and angle results from CPMD simulations for CO_2 absorption in $[\text{emim}][\text{CH}_3\text{COO}]$. The solid black line indicates the distance between the C atom of one CO_2 molecule and one O atom of one given $[\text{CH}_3\text{COO}]^-$ anion vs simulation time (left axis). The dotted red line corresponds to the $\theta(\text{OCO})$ for the same specific CO_2 molecule vs time (right axis). The regions with short $\text{C}(\text{CO}_2)-\text{O}([\text{CH}_3\text{COO}]^-)$ distances of about 1.4–1.8 Å and $\theta(\text{OCO})$ of 125–145° correspond to type I CO_2 absorption state. The remaining regions with distances larger than 2 Å and angles greater than 155° correspond to type II CO_2 absorption state. Two examples of type I and type II regions are also shown in the figure.

further performed to study CO_2 absorption in $[\text{emim}][\text{CH}_3\text{COO}]$. A typical snapshot from NVT CPMD simulations is shown in Figure 3. Two types of CO_2 absorption states were observed. Seven out of the 10 CO_2 molecules spend most of the time in a type I state and the other three CO_2 molecules spend most of the time in a type II state. Note that almost all 10 CO_2 molecules analyzed swap between type I and type II states during the 12 ps simulations. Type I and type II states indicated here refer to a highly bent, respectively to a slightly bent CO_2 configuration. These type I and II states observed in condensed-phase simulations correspond to the η^1 and η^2 structures in the gas-phase calculations. Representative geometric parameters for one of the CO_2 molecules interacting with a given $[\text{CH}_3\text{COO}]^-$ anion is shown in Figure 4. The $\theta(\text{OCO})$ for this specific CO_2 changes back and forth from about 135° corresponding to a type I state, to around 160° indicative of a type II state. During this process the C–O distance between the C atom of the CO_2 and one O atom of the $[\text{CH}_3\text{COO}]^-$ anion also swaps from about 1.60 Å (type I) to values larger than 2 Å (type II). Note that the angle and the distance variations correlate very well with each other; i.e., when the distance is smaller, the OCO angle is also smaller. These results indicate that a given CO_2 molecule can interact with the same $[\text{CH}_3\text{COO}]^-$ anion without drifting far away from this anion over the 12 ps simulations.

The angle distribution for all 10 CO_2 molecules is shown in Figure 5. Two distinct peaks are observed. The first peak covers a range from 120 to 152° and has a maximum at about 136°. This peak is assigned to a type I CO_2 absorption state as schematically shown on the left side in Figure 3. The second peak corresponding to a type II absorption state is centered at about 173° and varies in the range 152–180°.

For CO_2 in the type I state, the $\theta(\text{OCO})$, the intramolecular CO_2 bond length distributions and the distance between the C atom of CO_2 and O atoms of the $[\text{CH}_3\text{COO}]^-$ anion were also calculated and the corresponding distributions are shown in Figures 6 and 7. The average OCO angle and C–O bond length for CO_2 were calculated to be $137.6 \pm 1.7^\circ$ and 1.229 ± 0.001 Å. Both these two values deviate significantly from the 180° and

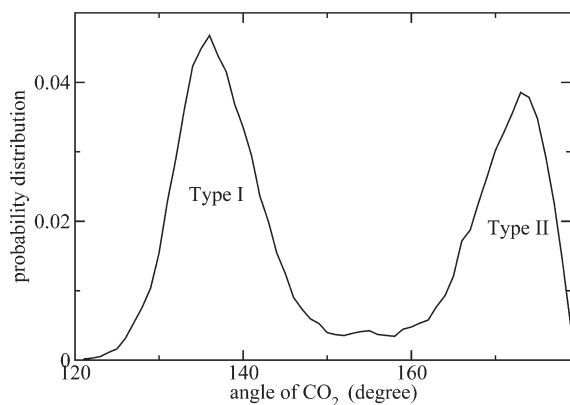


Figure 5. Angle distribution for all CO₂ molecules absorbed in [emim][CH₃COO] from CPMD simulations. The left and right peaks correspond to type I and type II absorption states for CO₂ interaction with the [CH₃COO][−] anion.

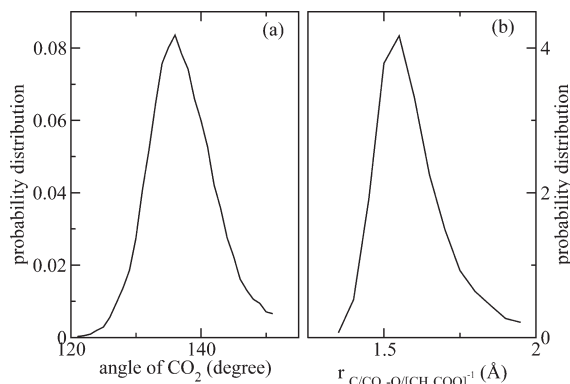


Figure 6. Probability distributions for CO₂ absorption in [emim][CH₃COO] in type I state as obtained from CPMD simulations: $\theta(\text{OCO})$ distribution (a) and the distance distribution between the C atom of CO₂ and an O atom of the [CH₃COO][−] anion (b).

1.16 Å values corresponding to an isolated CO₂ as obtained in ab initio gas-phase calculations. The average distance between a C atom of CO₂ and O atoms of the [CH₃COO][−] anion was computed to be 1.61 ± 0.04 Å. The distance distribution exhibits the largest probability at about 1.55 Å with a minimum value of 1.36 Å. The short distance between the C atom (CO₂) and the O atoms ([CH₃COO][−]) and the highly bent CO₂ configuration strongly indicate that in the type I state CO₂ interaction with the anion is strong, consistent with the large interaction energy between CO₂ and the [CH₃COO][−] anion given in Table 3 for the η^1 structure. From these results, it appears that the type I absorption state corresponds to the formation of a CO₂–[CH₃COO][−] complex, which leads to a high CO₂ solubility in [emim][CH₃COO].

For CO₂ in the type II state, the CO₂ molecules are located at greater distances from the [CH₃COO][−] anion than those in the type I state. The distance between the C atom of CO₂ and the O atoms of the [CH₃COO][−] anion is typically greater than 2.2 Å. The average OCO angle and C–O bond length (as shown in Figure 7) for CO₂ were calculated to be $170.7 \pm 1.9^\circ$ and 1.175 ± 0.001 Å, corresponding to a molecular configuration only slightly bent from a linear CO₂. The CO₂ molecular characteristics

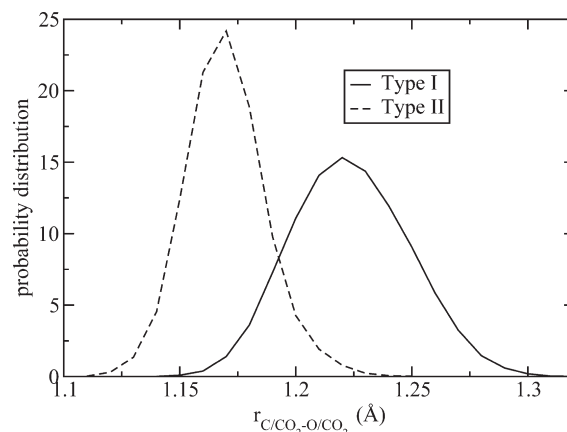


Figure 7. C–O (CO₂) bond length distributions for CO₂ absorption in [emim][CH₃COO] for type I and type II states as obtained from CPMD simulations.

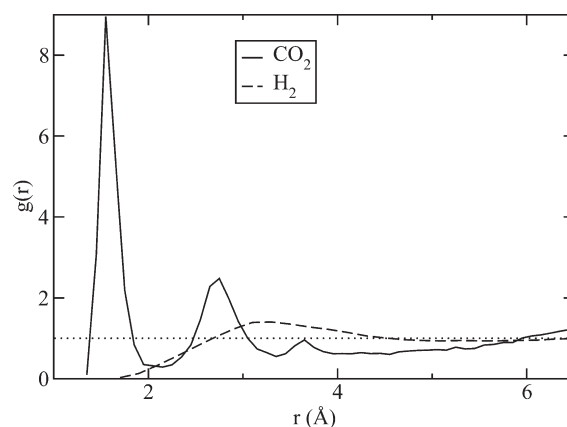


Figure 8. Radial distributions from CPMD simulations for CO₂/[emim][CH₃COO] and H₂/[emim][CH₃COO] systems. The solid line is for the distance between the C atom of CO₂ and O atoms of the [CH₃COO][−] anion. The dashed line indicates the distance distribution between H atoms of H₂ and all other atoms of the [emim][CH₃COO] ionic liquid. The horizontal dotted line corresponds to the radial distribution value of 1.

corresponding to the type II state are indicative of weak intermolecular interactions between CO₂ and the [CH₃COO][−] anion.

The above analysis only considers the interaction between CO₂ and the nearby anion. In order to understand the interactions between the CO₂ molecules and all the other anions in the system, the radial distribution function of the distance between the C(CO₂) and O([CH₃COO][−]) were calculated, and the result is shown in Figure 8. The radial distribution function exhibits two well-defined peaks. The first peak corresponding to the type I state occurs at about 1.55 Å, consistent with the distance distribution indicated in Figure 6b. The second peak representative of a type II state occurs at about 2.75 Å and corresponds to the interaction between CO₂ and the second shell of anions through weak intermolecular interactions. When the distance is larger than about 6 Å, the anions are randomly distributed around CO₂ molecules, as evidenced by the $g(r)$ distribution which is close to 1.

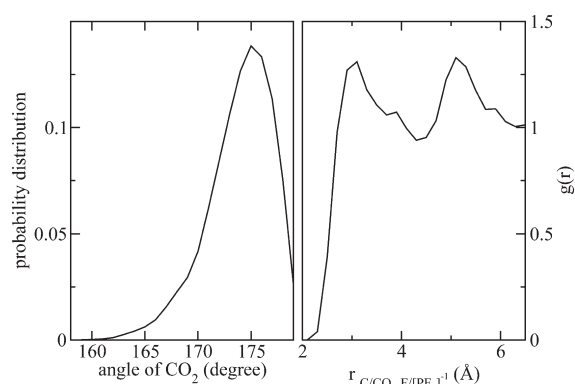


Figure 9. CO₂ bond angle distribution (left panel) and the radial distribution (right panel) for the distance between the C atom of CO₂ and the F atoms of the [PF₆][−] anion as obtained from CPMD simulations for CO₂ absorption in [emim][PF₆].

Effects of Functional and VDW Corrections. Two similar types of CO₂ absorption states were observed in CPMD simulations using the PBE functional. In these simulations, the OCO bond angle, the C–O bond distance, and the distance distributions between the C atom (CO₂) and the O atoms ([CH₃COO][−]) in type I and type II states were found to be similar to those obtained using the BLYP functions. The radial distribution function obtained for the PBE functional is also similar to that shown in Figure 8 for the BLYP functional. These results strongly suggest that both CO₂ geometries and the distribution functions shown in Figures 6, 7, and 8 are insensitive to the two types of functionals, i.e., BLYP and PBE.

The effect of including dispersion interactions in CPMD simulations was also studied using the Grimme³⁴ VDW corrections as implemented in the CPMD program. The simulations with and without VDW corrections (not shown here) also give similar CO₂ bond angles and bond lengths, distance distributions between the C atom (CO₂) and O atoms ([CH₃COO][−]), and radial distribution functions.

Weak Interaction between CO₂ and [emim][PF₆]. In the case of CO₂ absorption in [emim][PF₆], CPMD simulations show that all 10 CO₂ molecules are approximately linear and are located far away from the F atoms of the [PF₆][−] anion. The CO₂ bond angle and the radial distribution function for the C–(CO₂)–F([PF₆][−]) distance are shown in Figure 9. The average $\theta(\text{OCO})$ was found to be $174.4 \pm 0.5^\circ$, similar to the one observed for type II state for the CO₂–[emim][CH₃COO] system. The average C–O bond length was calculated to be 1.1720 ± 0.0004 Å, also very close to the value corresponding to the type II state for CO₂ absorption in [emim][CH₃COO]. The radial distribution function exhibits two peaks. The first peak occurs at about 3.0 Å, close to the value obtained from classical BH and AI gas-phase calculations as shown in Figure 2. The second peak occurs at about 5.0 Å. Both these two peaks reflect the existence of weak interactions between CO₂ molecules and the [PF₆][−] anions. These weak interactions indicated also in Table 3 are consistent with the small CO₂ solubility in [emim][PF₆].³³

Charge Transfer in the Condensed Phase. We also computed from CPMD simulations the charge transfer between the IL and CO₂ molecules in the condensed phase. In the case of the type I state, significant charge transfer from the [CH₃COO][−] anion to CO₂ was observed, leading to an average charge of about

Table 4. Variation of Solubility (α) and Mixture Molar Volume (V_{mix}) for H₂ Absorbed in [emim][CH₃COO] as Function of Temperature (T) and Pressure (P) As Obtained from Continuous Fractional Component Monte Carlo Simulations^a

T (K)	P (bar)	f (bar)	α	V_{mix} (cm ³ /mol)
313.2	200	221.8	0.025 (1)	156.3 (1)
313.2	400	492.8	0.042 (2)	152.7 (2)
323.2	200	214.0	0.023 (1)	157.2 (1)
323.2	400	465.6	0.044 (2)	153.6 (3)
348.2	200	213.6	0.025 (1)	159.3 (1)
348.2	400	463.2	0.049 (2)	155.2 (3)
373.2	200	219.4	0.029 (1)	160.9 (2)
373.2	400	481.2	0.052 (3)	156.4 (3)

^a Also shown in the table are the fugacity (f) values corresponding to the respective temperatures and pressures. The uncertainty in the last digit is given in parentheses.

−0.3 e for CO₂, close to the value of −0.4 e in the gas-phase-optimized η^1 structure. In the type II state, the charge transfer is insignificant and the average charge on CO₂ molecules was found to be about −0.02 e , close to the value of −0.1 e in the gas-phase η^2 structure. The significant charge transfer in the type I state is consistent with the strong interaction between CO₂ and the [CH₃COO][−] anion and the bent CO₂ structure. In the case of CO₂ absorption in [emim][PF₆], the charge transfer between the IL and CO₂ molecules was also found to be insignificant and the average charge on CO₂ molecules was computed to be −0.03 e . This small charge transfer is also consistent with the weak interaction obtained between CO₂ and [emim][PF₆] (see Table 3).

4.3. Results for H₂. **4.3.1. AI and BH Gas-Phase Calculations.** The H₂ interaction energies with three anions, [CH₃COO][−], [PF₆][−], [Tf₂N][−], and the [hmim]⁺ cation as obtained from AI and BH calculations are shown in Table 3. The AI calculations indicate that H₂ interacts most strongly with the [CH₃COO][−] anion. In contrast, the BH calculations indicate that H₂ interacts most strongly with the [Tf₂N][−] anion. Despite these differences, both AI and BH calculations give H₂ interaction energies much smaller than the CO₂ interaction energies with the same ions. These findings suggest small H₂ solubilities, results confirmed also by previous simulations and experiments for H₂ absorption in [hmim][Tf₂N] and [bmim][PF₆].^{8,35,36}

4.3.2. H₂ Absorption in [emim][CH₃COO] from CPMD Simulations. The radial distribution function between H atoms of H₂ and all atoms of [emim][CH₃COO] as obtained from CPMD simulations are shown in Figure 8. In this case, there is only one peak which occurs at about 3.2 Å. The large separation and the low peak height for this peak relative to the much shorter separation and the much higher peak height determined for type I CO₂ absorbed in [emim][CH₃COO] also indicate weak intermolecular interactions of H₂ with [emim][CH₃COO]. Based on this finding it is expected that H₂ solubility in [emim][CH₃COO] is low as is shown in the next section.

4.3.3. H₂ Solubility in [emim][CH₃COO] from Classical Simulations. H₂ solubilities in [emim][CH₃COO] obtained from classical CFC MC simulations in the temperature and pressure ranges 313.2–373.2 K and 200–400 bar are shown in Table 4. The Henry's law constant values, H , estimated from a linear fitting of the fugacity versus the solubility at low pressure, are $(1.2 \pm 0.2) \times 10^4$ bar at 313.2 K, $(1.06 \pm 0.08) \times 10^4$ bar at 323.2 K,

Table 5. van der Waals (VDW) Interaction Energies of H_2 – H_2 , H_2 – $[\text{emim}]^+$, and H_2 – $[\text{CH}_3\text{COO}]^-$ at a Temperature of 313.2 K and Pressures of 200 and 400 bar^a

P (bar)	x_{H_2}	VDW		
		H_2 – H_2 (kJ/mol)	H_2 – $[\text{emim}]^+$ (kJ/mol)	H_2 – $[\text{CH}_3\text{COO}]^-$ (kJ/mol)
200	0.024	$1(4) \times 10^{-3}$	–2.97(4)	–1.93(2)
400	0.048	$4(33) \times 10^{-4}$	–2.76(4)	–1.93(2)

^a The uncertainty in the last digit is given in parentheses.**Table 6.** Simulated Self-Diffusivity (D_s) Values for H_2 Absorption in $[\text{emim}][\text{CH}_3\text{COO}]$ at 313.2–372.2 K and Low H_2 Concentrations (x)

T (K)	x_{H_2}	D_{s,H_2} (m^2/s)	$D_{s,[\text{emim}]^+}$ (m^2/s)	$D_{s,[\text{CH}_3\text{COO}]^-}$ (m^2/s)
313.2	0.024	$(1.86 \pm 0.05) \times 10^{-9}$	$(1.06 \pm 0.03) \times 10^{-11}$	$(4.9 \pm 0.3) \times 10^{-12}$
323.3	0.048	$(2.06 \pm 0.02) \times 10^{-9}$	$(2.53 \pm 0.04) \times 10^{-11}$	$(1.36 \pm 0.02) \times 10^{-11}$
348.2	0.048	$(3.89 \pm 0.06) \times 10^{-9}$	$(6.59 \pm 0.05) \times 10^{-11}$	$(3.76 \pm 0.03) \times 10^{-11}$
373.2	0.048	$(4.0 \pm 0.1) \times 10^{-9}$	$(1.21 \pm 0.01) \times 10^{-10}$	$(6.8 \pm 0.2) \times 10^{-11}$

Table 7. Simulated and Experimental H_2 Permeability (Perm) in $[\text{emim}][\text{CH}_3\text{COO}]$ from 313.2 to 373.2 K^a

T (K)	sim H_2 perm (barrer)	expt		
		H_2 perm (barrer)	CO_2 perm (barrer)	CO_2/H_2 SELC
310.2	–	34 ± 3	1325 ± 73	37 ± 3
313.2	29 ± 6	–	–	–
323.2	36 ± 3	54 ± 1	1928 ± 98	36 ± 2
348.2	77 ± 5	113 ± 3	3293 ± 263	29 ± 3
373.2	79 ± 8	178 ± 8	3701 ± 103	21 ± 1

^a The experimental CO_2 permeability and CO_2/H_2 permeability selectivity (SELC) measured in this work are also included. The symbol – means that data are not available. Simulations suggest high CO_2 permeability and high CO_2/H_2 permeability selectivity.

$(9.4 \pm 0.5) \times 10^3$ bar at 348.2 K, and $(9.2 \pm 1.1) \times 10^3$ bar at 373.2 K. Note that the H values for H_2 in $[\text{emim}][\text{CH}_3\text{COO}]$ are very large, corresponding to a very small solubility. These H_2 solubility values in $[\text{emim}][\text{CH}_3\text{COO}]$ are about 6 times smaller than H_2 solubility in $[\text{hmim}][\text{Tf}_2\text{N}]$.⁸ The low H_2 solubility in $[\text{emim}][\text{CH}_3\text{COO}]$ is due to the small molar volume of $[\text{emim}][\text{CH}_3\text{COO}]$ (about half of that for $[\text{hmim}][\text{Tf}_2\text{N}]$), and the weak interactions between H_2 and the IL.

4.3.4. H_2 Interaction Energy with $[\text{emim}][\text{CH}_3\text{COO}]$. The interaction energies for H_2 – H_2 , H_2 – $[\text{emim}]^+$, and H_2 – $[\text{CH}_3\text{COO}]^-$ from classical MD simulations were computed by directly summing the pairwise interaction between the atoms in the primary cell and the neighboring 124 cells.³⁷ As shown in Table 5, the weak interaction energies between H_2 and $[\text{emim}][\text{CH}_3\text{COO}]$ are similar to those obtained from AI and BH gas-phase calculations, and are also consistent with the low H_2 solubility in $[\text{emim}][\text{CH}_3\text{COO}]$.

4.3.5. Self-Diffusivity of H_2 Absorption $[\text{emim}][\text{CH}_3\text{COO}]$. The self-diffusivity values (D_s) obtained from classical NVE MD simulations for H_2 , $[\text{emim}]^+$, and $[\text{CH}_3\text{COO}]^-$ are shown in Table 6. As observed in our previous work,⁸ the cation ($[\text{emim}]^+$) diffuses faster than the anion ($[\text{CH}_3\text{COO}]^-$). The H_2 diffuses about 1.7–2.1 times slower in $[\text{emim}][\text{CH}_3\text{COO}]$ than in $[\text{hmim}][\text{Tf}_2\text{N}]$.⁸ The slower H_2 diffusivity in $[\text{emim}][\text{CH}_3\text{COO}]$ may be partly due to its smaller IL molar volume than that for $[\text{hmim}][\text{Tf}_2\text{N}]$. When the temperature is increased from 313.2 to 373.2 K, the D_s value for $[\text{emim}][\text{CH}_3\text{COO}]$

increases by a factor of 10. In contrast, the D_s values for H_2 only double. Hence, the diffusion activation energy for the small H_2 solute molecule is much smaller than that for $[\text{emim}][\text{CH}_3\text{COO}]$. By assuming that the D_s value obeys simple Arrhenius behavior, the diffusion activation energy was estimated to be 13.9 ± 3.4 kJ/mol for H_2 , similar to the value of 14.6 ± 0.5 kJ/mol obtained for H_2 absorption in $[\text{hmim}][\text{Tf}_2\text{N}]$.⁸ For $[\text{emim}][\text{CH}_3\text{COO}]$, the diffusion activation energies were computed to be 38.0 ± 5.2 kJ/mol for $[\text{emim}]^+$ and 40.8 ± 6.7 kJ/mol for $[\text{CH}_3\text{COO}]^-$. We note that in most cases the $\beta = d(\log(\Delta r^2))/dt$ values for both H_2 and the ions are close to 1, indicative of diffusion regions.

4.3.6. H_2 Permeability in $[\text{emim}][\text{CH}_3\text{COO}]$. H_2 permeability in $[\text{emim}][\text{CH}_3\text{COO}]$ was calculated as in the previous work,⁸ and the results are shown in Table 7. The H_2 permeability in $[\text{emim}][\text{CH}_3\text{COO}]$ is very low, about 6 times smaller than the value for H_2 absorption in $[\text{hmim}][\text{Tf}_2\text{N}]$.⁸ Based on the low H_2 permeability and the high CO_2 solubility as shown above, the $[\text{emim}][\text{CH}_3\text{COO}]$ IL is predicted to exhibit high CO_2 permeability and large CO_2/H_2 permeability selectivity. These theoretical predictions were further tested through our experimental investigations as described in the next section.

4.4. Experimental CO_2 and H_2 Permeabilities in $[\text{emim}][\text{CH}_3\text{COO}]$. Our experimentally determined CO_2 and H_2 permeabilities in $[\text{emim}][\text{CH}_3\text{COO}]$ are shown in Table 7. In the case of H_2 , the experimental value agrees with the simulation at 310 K. At other temperatures of 323–373 K, experimental values are

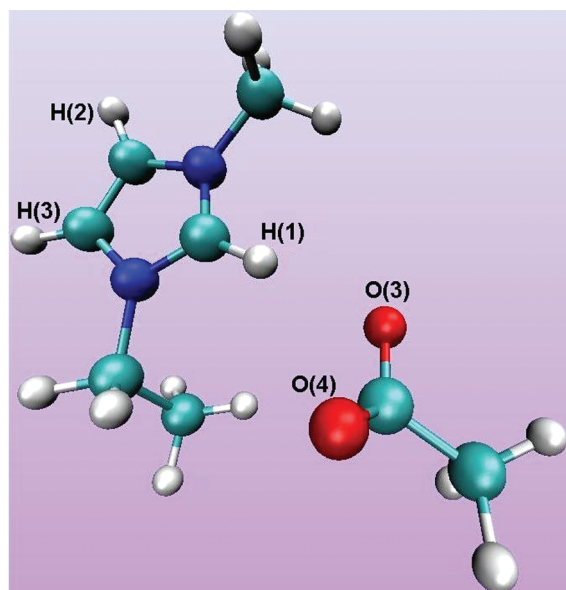


Figure 10. A snapshot of one pair of [emim][CH₃COO] ions from classical molecular dynamics simulations. For clarity, the rest of the ionic liquid molecules are not shown. The labels for the three hydrogen atoms on the [emim]⁺ cation ring and two oxygen atoms of [CH₃COO][−] referenced in this work are also indicated.

1.5–2.3 times larger than the simulated ones. The [emim][CH₃COO] IL exhibits higher CO₂ permeability and larger CO₂/H₂ permeability selectivity than the other two ILs ([hmim][Tf₂N] and [H₂NC₃H₆mim][Tf₂N]) as previously tested in our group.²⁹ These findings strongly indicate that simulations are very helpful in identifying promising ILs with improved performances for CO₂ capture.

4.5. Other ILs To Separate CO₂/H₂. **4.5.1. Competition between [emim]⁺ and CO₂ Interacting with [CH₃COO][−].** The above AI, BH, and CPMD simulations show that the primary interaction sites of CO₂ with the [CH₃COO][−] anion take place through the oxygen atoms of the [CH₃COO][−] anion. The strong interaction between the C atom of CO₂ and one O atom of the [CH₃COO][−] anion (η^1 configuration in the gas phase and type I state in the condensed phase) is responsible for the high CO₂ solubilities in [emim][CH₃COO]. In developing a comprehensive understanding of CO₂ interactions with acetate-based IL systems, it is also important to evaluate the role of cation–anion interactions upon CO₂ absorption.

A typical snapshot from classical MD simulations for the pure IL system is shown in Figure 10 and the corresponding radial distribution functions between H atoms of the [emim]⁺ cation and the O atoms of the [CH₃COO][−] anion are shown in Figure 11. The radial distribution for H(1)–O(4) (not shown) is similar to that for H(1)–O(3), and the ones for H(2)–O(4), H(3)–O(3), and H(3)–O(4) (not shown) are similar to that for H(2)–O(3). As shown in Figure 11, the H atoms of the [emim]⁺ cation interact with the O atoms of the [CH₃COO][−] anion. For H(1)–O(3), the first peak occurs at about 2.1 Å with a peak height of about 6. In the case of H(2)–O(3), the first peak occurs at about 2.4 Å with a maximum height of about 3. The strong interactions between the H(1) atom of the cation and O atoms of the anion are expected to compete with the CO₂–anion interaction and hence will decrease the CO₂ solubility in [emim][CH₃COO]. The H–O interactions are due to the positive

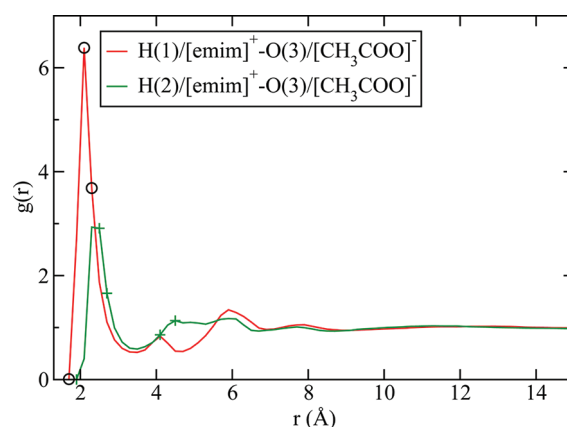


Figure 11. Radial distribution between the H atoms of the [emim]⁺ cation and the O atoms of the [CH₃COO][−] anion from classical molecular dynamics simulations of the pure [emim][CH₃COO] ionic liquid. The red solid line with circle symbols corresponds to the distance distribution between the H(1) atom of the [emim]⁺ cation and the O(3) atom of the [CH₃COO][−] anion. The green line with plus symbols is for H(2)–O(3). The numbers indicated in parentheses correspond to the atom labels shown in Figure 10.

charges of about +0.2e for the three H atoms (H(1), H(2), H(3)), and the negative charges of about −0.861e on the two O atoms (O(3), O(4)).

To verify the above competitive interactions from classical MD simulations, we analyzed CPMD simulations for the CO₂–[emim][CH₃COO] system. The radial distributions are shown in Figure 12. The first peak for H(1)–O(3) occurs at about 1.85 Å with a maximum height of about 3.6. In the case of C/CO₂–O/[CH₃COO][−], the peak occurs at about 1.56 Å with a peak height of about 9.0. There is a partial overlap between the two radial distributions in the region of the first peaks. This overlap strongly suggests that the H(1) atom of the cation competes with the C atom of CO₂ for the interaction with O atoms of the anion leading to a decrease of CO₂ solubility.

4.5.2. Separation of CO₂/H₂ Gas Mixtures Using [PY₁₄][CH₃COO]. As shown above, the H(1) atom of the [emim]⁺ cation competes for CO₂–[CH₃COO][−] interaction. We hypothesize that by replacing the [emim]⁺ cation with other cations that lack these types of H atoms might give a higher CO₂ solubility by decreasing the competitive cation–anion interactions. We analyze this hypothesis for the case of the 1-butyl-1-methylpyrrolidinium ([PY₁₄]⁺) cation and investigate the separation of CO₂ from H₂ using the [PY₁₄][CH₃COO] IL.

To evaluate the accuracy of the classical force-field parameters for the [PY₁₄]⁺ cation, the densities of [PY₁₄][Tf₂N] and [PY₁₄][CH₃COO] have been calculated based on classical MD simulations and the corresponding results are shown in Figure 13. The simulated densities for [PY₁₄][Tf₂N] are very close to the experimental values³⁸ with a difference of only about 1.3%. The small density differences imply that the force-field parameters for the [PY₁₄]⁺ cation and [Tf₂N][−] anion are effective in predicting the molar volume. For [PY₁₄][CH₃COO], there is no experimental density available for comparison.

As schematically shown in Figure 1, there are eight H atoms with small positive charges (ranging from +0.056e to +0.092e) attached to the [PY₁₄]⁺ five-membered ring. These small positive

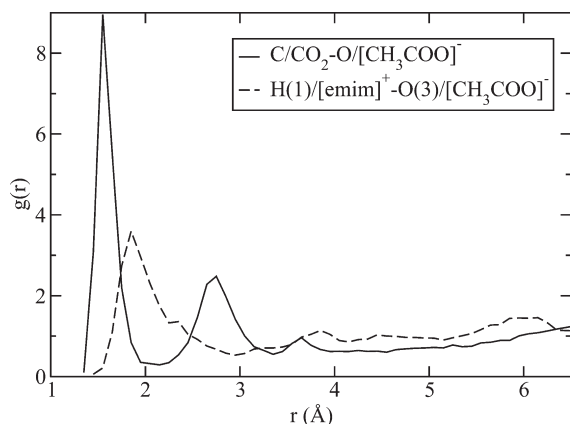


Figure 12. Radial distribution between the H(1) atom of the $[\text{emim}]^+$ cation and the O(3) atom of the $[\text{CH}_3\text{COO}]^-$ anion, and respectively between the C atom of CO_2 and O atoms of the $[\text{CH}_3\text{COO}]^-$ anion as obtained from CPMD simulations for CO_2 absorption in $[\text{emim}][\text{CH}_3\text{COO}]$. The numbers in parentheses correspond to the atom labels shown in Figure 10.

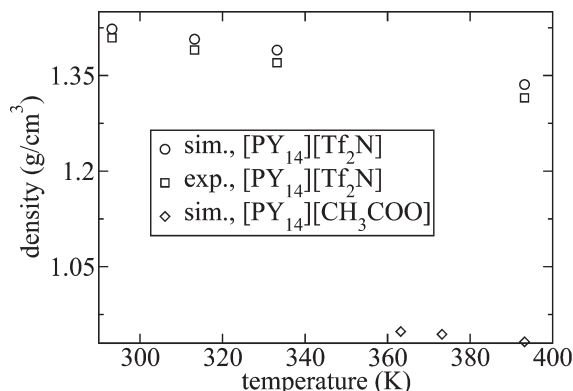


Figure 13. Simulated densities of $[\text{PY}_{14}][\text{Tf}_2\text{N}]$ and $[\text{PY}_{14}][\text{CH}_3\text{COO}]$. The error bars from simulations are typically smaller than the symbols and are not shown. For comparison, the experimental densities for $[\text{PY}_{14}][\text{Tf}_2\text{N}]$ ³⁸ are also shown.

charges will lead to weak electrostatic interactions with the O atoms of the $[\text{CH}_3\text{COO}]^-$ anion as shown in Figure 14. For clarity, only three representative radial distributions between atoms (N(13), C(27), H(28)) of the $[\text{PY}_{14}]^+$ cation and the O(3) atom of the $[\text{CH}_3\text{COO}]^-$ anion are shown. The first peaks for all these distributions exhibit lower peak heights and occur at larger distances than that for the H(1) atom of the $[\text{emim}]^+$ cation and the same O(3) atom of the $[\text{CH}_3\text{COO}]^-$ anion. These findings suggest that the $[\text{PY}_{14}]^+$ cation will interact more weakly than the $[\text{emim}]^+$ with the O atoms of the $[\text{CH}_3\text{COO}]^-$ anion. As a result, more O atoms of the $[\text{CH}_3\text{COO}]^-$ anion in the $[\text{PY}_{14}][\text{CH}_3\text{COO}]$ IL are available to interact with CO_2 leading to higher CO_2 solubility in $[\text{PY}_{14}][\text{CH}_3\text{COO}]$ than in $[\text{emim}][\text{CH}_3\text{COO}]$.

To investigate CO_2 absorption in $[\text{PY}_{14}][\text{CH}_3\text{COO}]$, we have also performed CPMD simulations. Similar to the case of CO_2 absorption in $[\text{emim}][\text{CH}_3\text{COO}]$, two types of CO_2 absorption states were observed (not show here). The observed type I state indicative of the strong CO_2 interaction with the $[\text{CH}_3\text{COO}]^-$

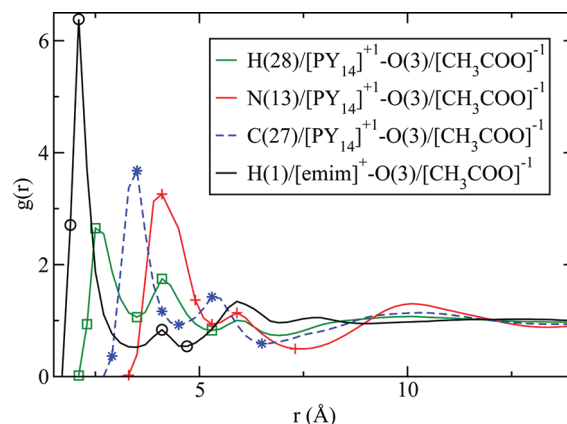


Figure 14. Radial distribution functions for the H(28), N(13), and C(27) atoms of the $[\text{PY}_{14}]^+$ cation and the O(3) atom of the $[\text{CH}_3\text{COO}]^-$ anion as obtained from classical molecular dynamics simulations of the pure ionic liquids, $[\text{emim}][\text{CH}_3\text{COO}]$ and $[\text{PY}_{14}][\text{CH}_3\text{COO}]$. For comparison, the radial distribution between the H(1) atom of the $[\text{emim}]^+$ cation and the same O(3) atom of the $[\text{CH}_3\text{COO}]^-$ anion is also shown. The legends for the lines are as follows: solid black line with circle symbols for $\text{H}(1)/[\text{emim}]^+-\text{O}(3)/[\text{CH}_3\text{COO}]^-$; green solid line with square symbols for $\text{H}(28)/[\text{PY}_{14}]^+-\text{O}(3)/[\text{CH}_3\text{COO}]^-$; blue dashed line with star symbols for $\text{C}(27)/[\text{PY}_{14}]^+-\text{O}(3)/[\text{CH}_3\text{COO}]^-$; and red solid line with cross symbols for $\text{N}(13)/[\text{PY}_{14}]^+-\text{O}(3)/[\text{CH}_3\text{COO}]^-$. The numbers indicated in the parentheses correspond to the atom labels shown in Figures 1 and 10.

Table 8. Solubility (x) and Mixture Molar Volume (V_{mix}) for H_2 in $[\text{PY}_{14}][\text{CH}_3\text{COO}]$ at Temperatures (T) in the Range of 363.2–393.2 K and Pressures (P) in the Range of 200–400 bar As Obtained from Continuous Fractional Component Monte Carlo Simulations^a

T (K)	P (bar)	f (bar)	x	V_{mix} (cm^3/mol)
363.2	200	213.4	0.019 (2)	206.2 (4)
363.2	400	461.6	0.045 (2)	199.9 (3)
373.2	200	219.4	0.023 (1)	206.0 (1)
373.2	400	481.2	0.041 (1)	201.2 (2)
393.2	200	213.0	0.021 (1)	207.9 (2)
393.2	400	458.4	0.040 (1)	202.8 (3)

^a Also shown in the table are the fugacity (f) values corresponding to the respective temperatures and pressures. The uncertainty in the last digit is given in parentheses.

anion suggests that CO_2 solubility in $[\text{PY}_{14}][\text{CH}_3\text{COO}]$ will be high.

The computed H_2 solubility values in $[\text{PY}_{14}][\text{CH}_3\text{COO}]$ are shown in Table 8. The Henry's law constants were estimated to be 10215 ± 471 bar at 363.2 K, 11637 ± 1416 bar at 373.2 K, and 11437 ± 798 bar at 393.2 K. These large Henry's law constants indicate very low H_2 solubility in $[\text{PY}_{14}][\text{CH}_3\text{COO}]$. Self-diffusivity for H_2 in $[\text{PY}_{14}][\text{CH}_3\text{COO}]$ was also calculated and found to be $(2.4 \pm 0.1) \times 10^{-9} \text{ m}^2/\text{s}$ at 373 K, while the corresponding permeability was estimated to be 29 ± 5 barrer, about 3 times smaller than the value for H_2 absorption in $[\text{emim}][\text{CH}_3\text{COO}]$. The low H_2 permeability and the expected high CO_2 solubility suggest that $[\text{PY}_{14}][\text{CH}_3\text{COO}]$ IL might be

a good candidate to separate CO₂ from H₂. These predictions await future experimental verification.

5. CONCLUSIONS

In this work, separations of CO₂ using [emim][CH₃COO] from mixtures containing H₂ have been investigated using both theoretical and experimental methods. Excepting for the η^1 configuration in the CO₂–[CH₃COO][−] dimer system, both ab initio and classical basin-hopping calculations show that in the gas-phase CO₂ interacts with the [CH₃COO][−] anion about 36%–151% more strongly than with the [PF₆][−] and [Tf₂N][−] anions. In the case of CO₂–[CH₃COO][−], ab initio calculations give a η^1 structure in which CO₂ is significantly bent and the interaction between CO₂ and the anion is very large. All these findings are consistent with the much higher CO₂ solubility in [CH₃COO][−]-based ILs compared to those based on the [PF₆][−] and [Tf₂N][−] anions. The CO₂–[hmim]⁺ interaction is weaker than those between CO₂ and the other three anions as indicated above. The interaction of H₂ with [CH₃COO][−], [PF₆][−], [Tf₂N][−], and [hmim]⁺ ions is much weaker than that for CO₂ with the same ions, consistent with the calculated low H₂ solubility and permeability in [emim][CH₃COO].

Although the classical force field gives an optimized structure for the CO₂–[CH₃COO][−] dimer system in the gas phase similar to η^2 configuration obtained from ab initio gas-phase calculation, it fails to predict the η^1 structure. This is due to the limitations of the current force field to describe the charge transfer from the [CH₃COO][−] anion to CO₂ molecule. These findings strongly suggest that a new force field model is required in this case to accurately describe the interaction between CO₂ and the [CH₃COO][−] anion.

For CO₂ absorption in [emim][CH₃COO], two types of CO₂ absorption states were observed from ab initio molecular dynamics simulations. In the type I state, the CO₂ molecule interacts with the [CH₃COO][−] anion through strong complexation. In this state, the C atom of CO₂ interacts strongly with O atoms of the [CH₃COO][−] anion leading to an average separation distance of about 1.61 Å. The average CO₂ bond angle in the type I state was found to be about 138°, and the average C–O bond length is elongated to about 1.23 Å, indicative of a significant bent CO₂ configuration relative to an isolated CO₂ molecule. In the type II state, CO₂ molecules interact with [emim][CH₃COO] through weak intermolecular interactions, similar to those observed for CO₂ absorption in [emim][PF₆]. The CO₂ bond angle and bond length in the type II state are similar to those for an isolated CO₂.

Simulations further show that the [emim]⁺ cation competes with CO₂ for interaction with the [CH₃COO][−] anion. It is proposed that replacing the [emim]⁺ cation with [PY₁₄]⁺ will lead to the availability of more O atoms of the [CH₃COO][−] anion to interact with CO₂. This substitution will in turn lead to an increase in CO₂ solubility. The H₂ solubility and permeability in [PY₁₄][CH₃COO] were calculated to be quite small, suggesting that [PY₁₄][CH₃COO] IL is a good candidate to separate CO₂ and H₂.

Experiments have also been performed to study CO₂ and H₂ separation using the [emim][CH₃COO] IL. The experimental CO₂ permeabilities in [emim][CH₃COO] range from 1325 to 3701 barrer, and the CO₂/H₂ permeability selectivities vary from 21 to 37 in the temperature range 313–373 K. The high CO₂ permeability and large CO₂/H₂ permeability selectivity verify

our theoretical predictions. The [emim][CH₃COO] was found to perform better than the other two ILs, i.e., [hmim][Tf₂N] and [H₂NC₃H₆mim][Tf₂N], previously tested in our group.²⁹

Although [emim][CH₃COO] performs well in terms of high CO₂ permeability and larger CO₂/H₂ permeability selectivity, there are other factors that have to be considered. One example is the amount of water present in both pre- and postcombustion CO₂ capture streams and its effects on the separation and stability of the IL. Questions of this type will be addressed in future studies. In spite of these, this work further supports our original findings⁸ that ILs with small molar volume (leading to low H₂ solubility) which interact with CO₂ strongly (leading to high CO₂ solubility) may be the best candidates for CO₂ separations from mixtures containing H₂. This is indeed what we found using [emim][CH₃COO] to separate CO₂ and H₂.

AUTHOR INFORMATION

Corresponding Author

*E-mail: shiw@netl.doe.gov (W.S.); david.luebke@netl.doe.gov (D.R.L.).

ACKNOWLEDGMENT

This technical effort was performed in support of the National Energy Technology Laboratory's ongoing research in computational chemistry under the RES contract DE-FE0004000.

REFERENCES

- (1) Maginn, E. J. *Design and Evaluation of Ionic Liquids as Novel CO₂ Absorbents*. <http://www.netl.doe.gov/technologies/coalpower/ewr/co2/pubs> (accessed Oct 5, 2011).
- (2) Chinn, D.; Vu, D. Q.; Driver, M. S.; Boudreau, L. C. CO₂ removal from gas using ionic liquid absorbents. U.S. Patent 20,060,251,558A1, November 9, 2005; 20,050,129,598A1, June 16, 2005.
- (3) Yokozeki, A.; Shiflett, M. B.; Junk, C. P.; Grieco, L. M.; Foo, T. *J. Phys. Chem. B* **2008**, *112*, 16654–16663.
- (4) Shiflett, M. B.; Kasprzak, D. J.; Junk, C. P.; Yokozeki, A. *J. Chem. Thermodyn.* **2008**, *40*, 25–31.
- (5) Shiflett, M. B.; Yokozeki, A. *J. Chem. Eng. Data* **2009**, *54*, 108–114.
- (6) Bhargava, B. L.; Balasubramanian, S. *Chem. Phys. Lett.* **2007**, *444*, 242–246.
- (7) Carvalho, P. J.; Alvarez, V. H.; Schroder, B.; Gil, A. M.; Marrucho, I. M.; Aznar, M.; Santos, L. M. N. B. F.; Coutinho, J. A. P. *J. Phys. Chem. B* **2009**, *113*, 6803–6812.
- (8) Shi, W.; Sorescu, D. C.; Luebke, D. R.; Keller, M. J.; Wickramanayake, S. *J. Phys. Chem. B* **2010**, *114*, 6531–6541.
- (9) Allen, M. P.; Tildesley, D. J. *Computer Simulation of Liquids*; Clarendon: Oxford, UK, 1987.
- (10) Cadena, C.; Anthony, J. L.; Shah, J. K.; Morrow, T. I.; Brennecke, J. F.; Maginn, E. J. *J. Am. Chem. Soc.* **2004**, *126*, 5300–5308.
- (11) Liu, Z. P.; Wu, X. P.; Wang, W. C. *Phys. Chem. Chem. Phys.* **2006**, *8*, 1096–1104.
- (12) Shi, W.; Maginn, E. J. *J. Phys. Chem. B* **2008**, *112*, 2045–2055.
- (13) Shi, W.; Maginn, E. J. *AIChE J.* **2009**, *55*, 2414–2421.
- (14) Canongia Lopes, J. N.; Padua, A. A. H. *J. Phys. Chem. B* **2006**, *110*, 19586–19592.
- (15) Cracknell, R. F. *Phys. Chem. Chem. Phys.* **2001**, *3*, 2091–2097.
- (16) Jorgensen, W.; Maxwell, D.; Tirado-Rives, J. *J. Am. Chem. Soc.* **1996**, *118*, 11225–11236.
- (17) Frisch, M. J.; Trucks, G. W.; Schlegel, H. B.; Scuseria, G. E.; Robb, M. A.; Cheeseman, J. R.; Montgomery, Jr., J. A.; Vreven, T.;

Kudin, K. N.; Burant, J. C. et al. *Gaussian 03, Revision C.02*; Gaussian, Inc.: Wallingford, CT, 2004.

(18) Wales, D. J.; Doye, J. P. K. *J. Phys. Chem. A* **1997**, *101*, 5111–5116.

(19) Wales, D. J.; Scheraga, H. A. *Science* **1999**, *285*, 1368–1372.

(20) LaBrosse, M. R.; Shi, W.; Johnson, J. K. *Langmuir* **2008**, *24*, 9430–9439.

(21) Fennell, C. J.; Gezelter, J. D. *J. Chem. Phys.* **2006**, *124*, 234104.

(22) Breneman, C. M.; Wiberg, K. B. *J. Comput. Chem.* **1990**, *11*, 361–373.

(23) Shao, Y.; Molnar, L. F.; Jung, Y.; Kussmann, J.; Ochsenfeld, C.; Brown, S. T.; Gilbert, A. T. B.; Slipchenko, L. V.; Levchenko, S. V.; O'Neill, D. P. *Phys. Chem. Chem. Phys.* **2006**, *8*, 3172–3191.

(24) Car, R.; Parrinello, M. *Phys. Rev. Lett.* **1985**, *55*, 2471–2474.

(25) Hutter, J.; Ballone, P.; Bernasconi, M.; Focher, P.; Fois, E.; Goedecker, S.; Marx, D.; Parrinello, M.; Tuckerman, M. E. *CPMD, version 3.13.2*; Max Planck Institut für Festkörperforschung: Stuttgart, Germany, 1990–2008.

(26) Taguchi, R.; Machida, H.; Sato, Y.; Smith, R. L. *J. Chem. Eng. Data* **2009**, *54*, 22–27.

(27) Hirshfeld, F. L. *Theor. Chim. Acta* **1977**, *44*, 129–138.

(28) Singh, U. C.; Kollman, P. A. *J. Comput. Chem.* **1984**, *5*, 129–145.

(29) Myers, C.; Pennline, H.; Luebke, D.; Ilconich, J.; Dixon, J. K.; Maginn, E. J.; Brennecke, J. F. *J. Membr. Sci.* **2008**, *322*, 28–31.

(30) Simons, K.; Nijmeijer, K.; Bara, J. E.; Noble, R. D.; Wessling, M. *J. Membr. Sci.* **2010**, *360*, 202–209.

(31) Shah, J. K.; Maginn, E. J. *J. Phys. Chem. B* **2005**, *109*, 10395–10405.

(32) Anthony, J. L.; Maginn, E. J.; Brennecke, J. F. *J. Phys. Chem. B* **2002**, *106*, 7315–7320.

(33) Shariati, A.; Peters, C. J. *J. Supercrit. Fluids* **2004**, *29*, 43–48.

(34) Grimme, S. *J. Comput. Chem.* **2006**, *27*, 1787–1799.

(35) Kumelan, J.; Kamps, Á. P. S.; Tuma, D.; Maurer, G. *J. Chem. Eng. Data* **2006**, *51*, 1364–1367.

(36) Kumelan, J.; Kamps, Á. P. S.; Tuma, D.; Maurer, G. *J. Chem. Eng. Data* **2006**, *51*, 11–14.

(37) Shi, W.; Maginn, E. J. *J. Phys. Chem. B* **2008**, *112*, 16710–16720.

(38) Gardas, R.; Costa, H.; Freire, M.; Carvalho, P.; Marrucho, I.; Fonseca, I.; Ferreira, A.; Coutinho, J. *J. Chem. Eng. Data* **2008**, *53*, 805–811.